MNRAS **000**, 000–000 (0000) Preprint May 14, 2019 Compiled using MNRAS LATEX style file v3.0

Gravitational waves from three-dimensional core-collapse supernova models: The impact of moderate progenitor rotation

H. Andresen[1,2,3⋆], E. Müller[1], H.-Th. Janka[1], A. Summa[1], K. Gill[4,5], and M. Zanolin[6]
[1]*Max-Planck-Institut für Astrophysik,Karl-Schwarzschild-Str. 1, D-85748 Garching, Germany*
[2]*Physik Department, Technische Universität München, James-Franck-Str. 1, 85748 Garching, Germany*
[3] *Max Planck Institute for Gravitational Physics (Albert Einstein Institute), Am Mühlenberg 1, Potsdam-Golm, 14476, Germany*
[4]*Harvard-Smithsonian Center for Astrophysics, 60 Garden Street, Cambridge, Massachusetts 02138, USA*
[5]*Department of Physics, Columbia University, New York, New York 10027, USA*
[6]*Embry Riddle University, 3700 Willow Creek Road, Prescott, Arizona 86301, USA*

May 14, 2019

ABSTRACT

We present predictions for the gravitational-wave (GW) emission of three-dimensional supernova (SN) simulations performed for a 15 solar-mass progenitor with the PROMETHEUS-VERTEX code using energy-dependent, three-flavor neutrino transport. The progenitor adopted from stellar evolution calculations including magnetic fields had a fairly low specific angular momentum ($j_{\rm Fe} \lesssim 10^{15}\,{\rm cm^2 s^{-1}}$) in the iron core (central angular velocity $\Omega_{\rm Fe,c} \sim 0.2\,{\rm rad\,s^{-1}}$), which we compared to simulations without rotation and with artificially enhanced rotation ($j_{\rm Fe} \lesssim 2\times10^{16}\,{\rm cm^2 s^{-1}}$; $\Omega_{\rm Fe,c} \sim 0.5\,{\rm rad\,s^{-1}}$). Our results confirm that the time-domain GW signals of SNe are stochastic, but possess deterministic components with characteristic patterns at low frequencies ($\lesssim$200 Hz), caused by mass motions due to the standing accretion shock instability (SASI), and at high frequencies, associated with gravity-mode oscillations in the surface layer of the proto-neutron star (PNS). Nonradial mass motions in the postshock layer as well as PNS convection are important triggers of GW emission, whose amplitude scales with the power of the hydrodynamic flows. There is no monotonic increase of the GW amplitude with rotation, but a clear correlation with the strength of SASI activity. Our slowly rotating model is a fainter GW emitter than the nonrotating model because of weaker SASI activity and damped convection in the postshock layer and PNS. In contrast, the faster rotating model exhibits a powerful SASI spiral mode during its transition to explosion, producing the highest GW amplitudes with a distinctive drift of the low-frequency emission peak from ∼80–100 Hz to ∼40–50 Hz. This migration signifies shock expansion, whereas non-exploding models are discriminated by the opposite trend.

Key words: gravitational waves – supernovae: general – hydrodynamics – instabilities

1 INTRODUCTION

Gavitational waves (GW) are generated in core-collapse supernovae by time-dependent rotational flattening particularly during collapse and bounce, prompt post-shock convection, non-radial flow inside the proto-neutron star and in the neutrino-heated hot bubble, the activity of the standing accretion shock instability (SASI), asymmetric emission of neutrinos, and by asymmetries associated with the effects of magnetic fields (for recent reviews see, *e.g.,* Fryer & New 2011; Kotake 2013; Müller 2017). Measurable impact of rotation on the GW signature is only expected for particular progenitors that possess a sufficient amout of angular momentum, while all other processes are genuinely operative in any core-collapse supernova.

Although, the rotation rate of most core-collapse progenitors might be slow rather than rapid (Heger et al. 2005; Beck et al. 2012; Mosser et al. 2012; Popov & Turolla 2012; Noutsos et al. 2013; Cantiello et al. 2014; Deheuvels et al. 2014), the study of GW generated by the core-collapse of rotating stars has a long and rich history (for a review see, *e.g.,* Fryer & New 2011; Kotake 2013). Most earlier studies of the GW signature of core-collapse supernovae were concerned only with the collapse, bounce, and early ($\lesssim$ 20 ms) post-bounce evolution of a rotating iron core assuming axisymmetry (see, *e.g.,* Müller 1982; Mönchmeyer et al. 1991; Zwerger & Müller 1997; Dimmelmeier et al. 2002; Kotake et al. 2003; Shibata & Sekiguchi 2004; Dimmelmeier et al. 2007, 2008) or none (see, *e.g.,* Rampp et al. 1998; Shibata & Sekiguchi 2005; Ott et al. 2007; Scheidegger et al. 2010b). Studies of the influence of rotation (and of a magnetic field) on the GW signal from the phase of neutrino-driven convection and SASI, and the onset of explosion

⋆ E-mail: haakon.andresen@aei.mpg.de

or black hole formation have become available more recently (Ott et al. 2011; Kotake et al. 2011; Ott et al. 2012a; Cerdá-Durán et al. 2013; Kuroda et al. 2014; Yokozawa et al. 2015; Hayama et al. 2016; Takiwaki & Kotake 2018). They showed that a dominant source of post-bounce GW emission in rotating cores is due to non-axisymmetric instabilities, which also have an important influence on the explosion (Kotake et al. 2011; Kuroda et al. 2014; Takiwaki et al. 2016; Takiwaki & Kotake 2018). All of these 3D GW signal predictions rely on a simplified treatment of neutrino transport. Up to now, only Summa et al. (2018) have provided self-consistent 3D models for a rotating progenitor, but the GW signature of these models will only be discussed in this paper.

For a more rapidly rotating case than considered by Summa et al. (2018), the post-bounce GW signal shows clear imprints of non-axisymmetric instabilities arising from the low-T/W instability (Takiwaki et al. 2016; Takiwaki & Kotake 2018). This 3D instability leads to a pole-to-equator contrast in the GW amplitudes. The emission, peaking at about 240 Hz, is stronger along the spin axis of the rotating core, and the amplitude contrast is larger for the h_x polarization mode than for the h_+ mode (Takiwaki & Kotake 2018). This result confirms earlier findings which were obtained in simulations using a more approximate neutrino transport (Ott 2009; Scheidegger et al. 2010b). The GW frequency is twice the modulation frequency of the neutrino signal, and hence joint GW and neutrino observations could provide evidence for or against rapid core rotation (Ott et al. 2012b; Yokozawa et al. 2015; Kuroda et al. 2017; Takiwaki & Kotake 2018). These GW signal predictions were obtained, however, from 3D models with an initial pre-collapse angular frequency of $\Omega_0 = 2$ rad/s in the iron core and with simplified treatment of neutrino transport.

Here, we present the GW signals from three 3D core-collapse simulations performed by Summa et al. (2018) to study the possible support of neutrino-driven supernova explosions by more modest rotation. These self-consistent 3D simulations applied the most complete set of neutrino interactions currently available, and are based on the spherically symmetric $15M_\odot$ progenitor model m15u6 from stellar evolution calculations by Heger et al. (2005) [1] , which was evolved in 1D including the effects of rotation and angular momentum transport by magnetic fields. Summa et al. (2018) also performed two additional core-collapse simulations for the same progenitor. In one model the rate of rotation was increasing to $\Omega_0 = 0.5$ rad/s in the central iron core. In the second additional simulation the initial rotation rate was set to zero throughout the stellar progenitor. model. We have also evaluated the GW signal of these two models. The 3D simulations of Summa et al. (2018) start only approximately 10 ms after core bounce (the earlier evolution was simulated in axisymmetry), because deviations from axisymmetry should not occur until this time for the moderately fast rotating progenitors they adopted for their work. Hence, the expected GW signal associated with core bounce of the two rotating models was obtained from axisymmetric configurations. Analyzing the GW signature of the three models allows us study how the signal changes, for the same stellar progenitor, as a function of progenitor rotation. The fastest rotating model and the model without rotation are dominated by strong SASI activity, while the slowly rotating model develops only weak and intermittent SASI oscillations, *i.e.,* we can also ascertain the influence of rotation in both the SASI dominated regime and the convective regime on the GW signal.

The paper is structured as follows: First, we recap the numerical methods and input physics used in the code of Summa et al. (2018) to perform the numerical simulations of the 3D supernova models. In section 3, we describe the relevant properties of the models of Summa et al. (2018) that we have analyzed for their GW signature, and we briefly discuss their dynamics. The formalism we used to extract the GW signature from the models of Summa et al. (2018) is described in section 4. In sections 5, 6, 8, and 9 we present the GW signals, discussing the underlying hydrodynamic effects responsible for GW excitation and how these effects are affected by rotation. We briefly discuss the GW signal associated with core bounce (simulated only in 2D; see above) for completeness.

Before we give our conclusions in section 11, we assess the detection prospects for the GW signals of the three models analyzed by us in section 10.

2 NUMERICAL METHODS AND INPUT PHYSICS

The PROMETHEUS-VERTEX code (Rampp & Janka 2002; Buras et al. 2006a) was used to perform the core-collapse simulations of Summa et al. (2018). PROMETHEUS-VERTEX consists of two main modules. The hydrodynamics calculations are handled by PROMETHEUS (Müller et al. 1991; Fryxell et al. 1991), which is a Newtonian hydro-code that implements the piecewise parabolic method of Colella & Woodward (1984) in spherical coordinates (r, θ, ϕ). The monopole approximation is used to treat self-gravity and general relativistic effects are taken into account by means of a pseudo-relativistic potential (case A of Marek et al. 2006). The neutrino transport is taken care of by the module VERTEX (Rampp & Janka 2002), which solves the energy-dependent two-moment equations for three neutrino species, electron neutrinos (ν_e), anti-electron neutrinos ($\bar{\nu}_e$), and a third species (ν_X) representing all the heavy flavor neutrinos, using a variable Eddington-factor closure computed from solutions of the Boltzmann equation. Multi-dimensional transport is approximated by the "ray-by-ray-plus" method of Buras et al. (2006a). The high-density equation of state (EoS) used is the nuclear equation of state (EoS) of Lattimer & Swesty (1991), with $K = 220\,\mathrm{MeV}$. Below $10^{11}\,\mathrm{g/cm^3}$ a low-density EoS for nuclei, nucleons, charged leptons and photons is applied.

3 SUPERNOVA MODELS

We extracted the GW signal of three models of Summa et al. (2018) based on the progenitor of Heger et al. (2005), which is a solar-metallicity star with a zero-age main sequence (ZAMS) mass of 15 solar masses ($M_\odot$). The stellar evolution calculation of Heger et al. (2005) accounted for the effects of magnetic fields and rotation, they evolved the model from the ZAMS to the onset of core-collapse. The inclusion of magnetic fields leads to a dramatic overall reduction of the final rotation rate of the iron core, compared to calculations without magnetic fields.

Summa et al. (2018) carried out five 3D simulations of the core-collapse of the progenitor star with different initial rotation profiles and different angular resolutions (see their Table 1). In two models of different angular resolution the rotation profile dictated by the stellar evolution calculations of Heger et al. (2005) was used. In another model Summa et al. (2018) used an arteficially enhanced rotation rate and a modified rotation profile. Finally, they simulated two 3D models of different angular resolution where the initial rotation rate was set to zero throughout the star, *i.e.,* these two models

[1] http://www.2sn.org/stellarevolution/magnet/

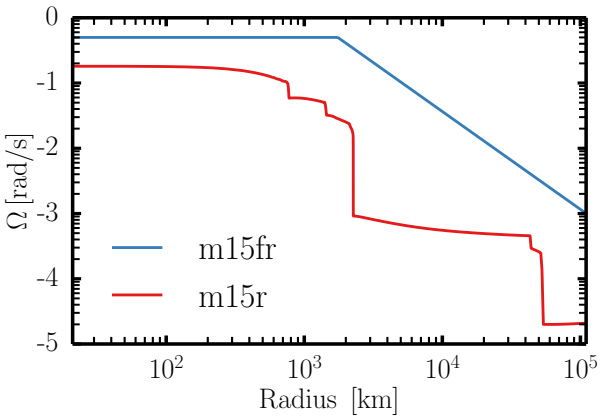

Figure 1. Pre-collapse rotation profiles (Summa et al. (2018) assumed the angular velocity to be constant on spheres) for the two rotating models m15fr and m15r, respectively. Both the x-axis and y-axis are shown in logarithmic scale.

were non-rotating. Fig. 1 shows the initial rotation profiles of the rotating models.

For our study we selected the three models with the best angular resolution, *i.e.,* models m15_3D_artrot_2deg, m15_3D_rot_2deg, and m15_3D_norot_4deg (see Table 1 in Summa et al. (2018)). In the following we will use the shorthand model notation m15fr, m15r, and m15nr, respectively, for these three models. The ending of the model names indicates the rotation rate (fr: **f**ast **r**otating , nr: **n**on **r**otating, and r: slowly **r**otating).

Model m15fr: The initial rotation profile of model m15fr was set to a constant rotation rate of 0.5 rad/s throughout the inner 1731 km of the core, while beyond this radius the rotation rate declines linearly (Fig. 1). The model was simulated using the Yin-Yang grid, the two grid patches had an initial resolution of 400, 56, and 144 zones in radial, polar, and azimuthal direction, respectively. This corresponds to a 2-degree angular resolution. The number of radial grid cell was increased during the simulation. After the initial shock expansion halts, around 60 ms post bounce, the average shock radius decreases slightly. Between $\sim 80 - 160$ ms post bounce the shock front is more or less stationary. The shock starts to expand again at about 160 ms after core bounce and soon afterwards shock revival sets in. Before shock revival the post-shock flow is dominated by a strong spiral SASI mode. The SASI sets in at around $\sim$ 100 ms post bounce. In Fig. 2 we show volume renderings of the entropy per nucleon, which gives an impression of the flow patterns of this model.

Model m15r: The initial rotation profile of model m15r (see Fig. 1) was exactly that of the progenitor of (Heger et al. 2005). The model was simulated using the Yin-Yang grid, the two grid patches had an initial resolution of 400, 56, and 144 zones in the radial, polar, and azimuthal direction, respectively. This corresponds to a 2-degree angular resolution. The number of radial grid cell was increased during the simulation. For the first $\sim$ 80 ms after bounce the evolution of the average shock radius closely resembles that of model m15fr. However, around 100 ms after bounce the average shock radius starts to decrease. Only very weak, compared to the other two models, SASI oscillations develop in this model. The flow in the post-shock region is instead dominated by hot-bubble convection (see Fig. 3). However, between $\sim$ 200 and 260 ms after bounce there is a period of low-amplitude dipole deformation of the shock front (see Fig. 5). The decrease of the average shock radius, which started around 100 ms after bounce, continues until $\sim$ 200 ms post bounce when the Si-O shell interface falls through the shock. The decreased density ahead of the shock reduces the ram pressure and a transient period of shock expansion occurs. About 240 ms post bounce the expansion subsides and the shock front once more begins to retreat, a trend which continues until the end of the simulation.

Model m15nr: In model m15nr the initial rotation rate was set to zero at all radii. The model was simulated using the Yin-Yang grid, the two grid patches had an initial resolution of 400, 28, and 72 zones in radial, polar, and azimuthal direction, respectively. This means that model m15nr was simulated with an angular resolution that is two times coarser than the other two models (4 degrees instead of 2 degrees). The number of radial grid cell was increased during the simulation. The lower angular resolution discourages neutrino-driven convection and is conducive to the development of SASI activity. Initially, the shock expands and reaches a local maximum around 60 ms after bounce. Later on the shock radius steadily decreases until the Si-O shell interface falls through the shock. The decreased accretion rate leads to a transient period of shock expansion until the shock eventually starts to recede once again. Except for the fact that the average shock radius at late times is generally larger in model m15nr than in model m15r, model m15nr behaves similarly to model m15r in terms of the evolution of the average shock radius. However, unlike model m15r, model m15nr develops strong SASI activity, which is dominated by the spiral mode. The mode develops at about 120 ms after core bounce and peaks at $\sim$ 230 ms post bounce. Afterwards the SASI mode gradually decays towards the end of the simulation.

Note that the coefficients given in Fig. 4 and Fig. 5 are defined as

$$a_l^m(t_n) = \frac{(-1)^{|m|}}{\sqrt{4\pi(2l+1)}} \int r_{\rm sh}(\theta,\phi,t) Y_l^m d\Omega, \qquad (1)$$

where $r_{\rm sh}$ is the shock position , and Y_l^m is the spherical harmonic of degree l and order m.

4 GRAVITATIONAL WAVE EXTRACTION

The GW signals are extracted from the hydrodynamical simulations by post-processing the output data using the quadrupole stress formula (Finn 1989; Nakamura & Oohara 1989; Blanchet et al. 1990). The formalism is described in detail in, for example, Finn (1989). Here we will give only the final formula.

The expressions for the two independent components, h_+ and $h_\times$, of the gravitational wave tensor at observer distance D in the transverse traceless (TT) gauge for a wave propagating into a general direction given by the spherical polar coordinates $(r,\ \theta,\ \phi)$ are

$$\begin{aligned} h_+ = \frac{G}{c^4 D}\Big[& \ddot{Q}_{11}(\cos^2\phi - \sin^2\phi\cos^2\theta) \\ & + \ddot{Q}_{22}(\sin^2\phi - \cos^2\phi\cos^2\theta) - \ddot{Q}_{33}\sin^2\theta \\ & - \ddot{Q}_{12}(1+\cos^2\theta) + \ddot{Q}_{13}\sin\phi\sin 2\theta \\ & + \ddot{Q}_{23}\cos\phi\sin 2\theta\Big] \end{aligned} \qquad (2)$$

and

$$\begin{aligned} h_\times = \frac{G}{c^4 D}\Big[& (\ddot{Q}_{11} - \ddot{Q}_{22})\sin 2\phi\cos\theta \\ & + \ddot{Q}_{12}\cos\theta\cos 2\phi - \ddot{Q}_{13}\cos\phi\sin\theta \\ & + 2\ddot{Q}_{23}\sin\phi\sin\theta\Big]. \end{aligned} \qquad (3)$$

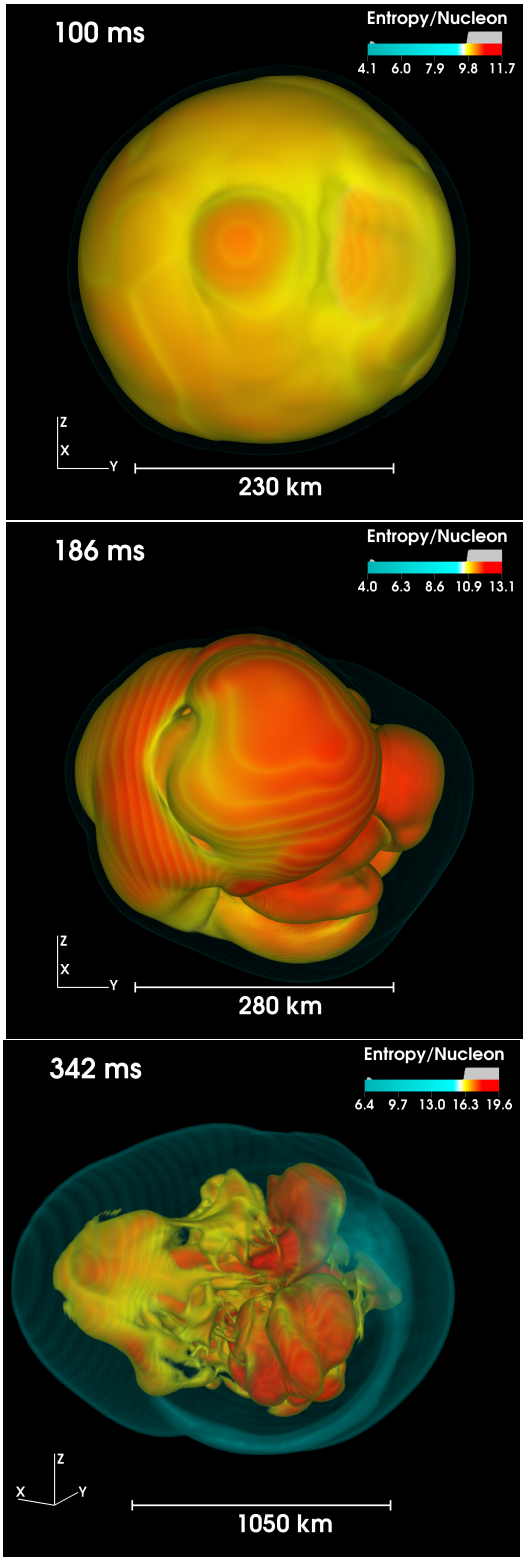

Figure 2. Volume rendering of the entropy per nucleon for model m15fr at three different times, the time after core bounce is indicated in the upper left corner of each panel. The blue surface shows the shock front. The deformation of the shock front, which is indicative of SASI activity, can be seen in the middle panel. In the bottom panel the average shock radius has reached large values and runaway shock expansion is underway.

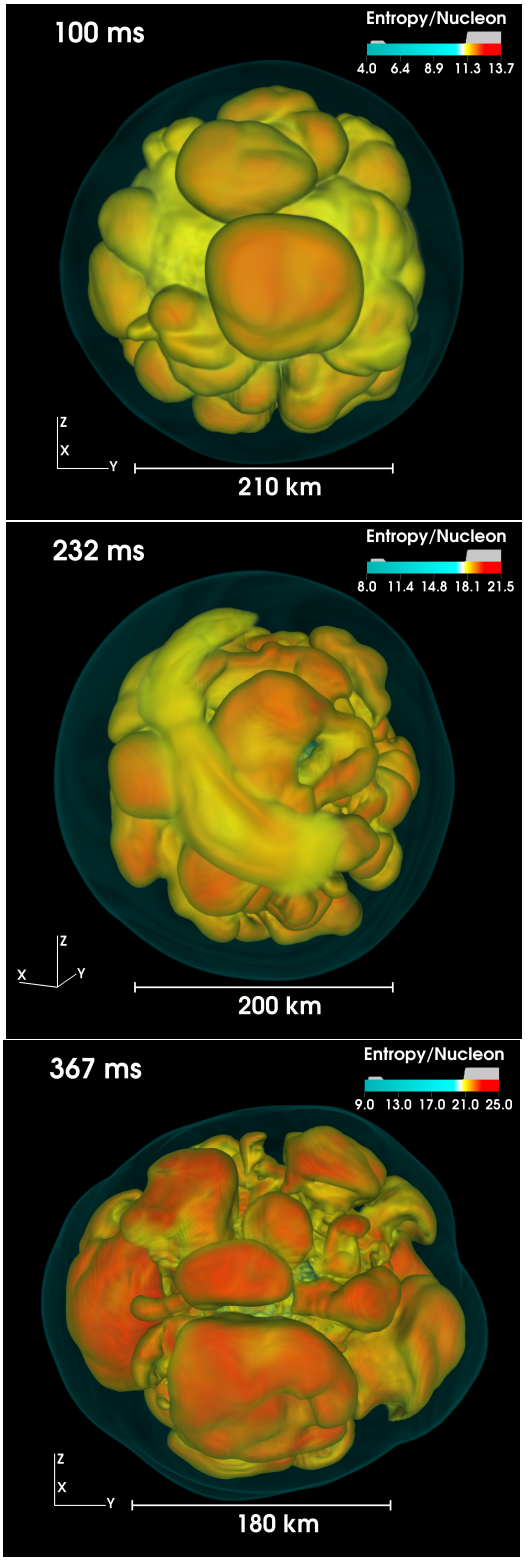

Figure 3. Volume rendering of the entropy per nucleon for model m15r at three different times, the time after core bounce is indicated in the upper left corner of each panel. The blue surface shows the shock front. In all panels, the flow in the region between the shock and the PNS is dominated by neutrino-driven convection, the typical mushroom shaped convective bubbles being clearly visible. However, in the middle panel the convective activity is severely reduced. The yellow arc seen in this panel is a sign of weak SASI activity, which intermittently develops in model m15r.

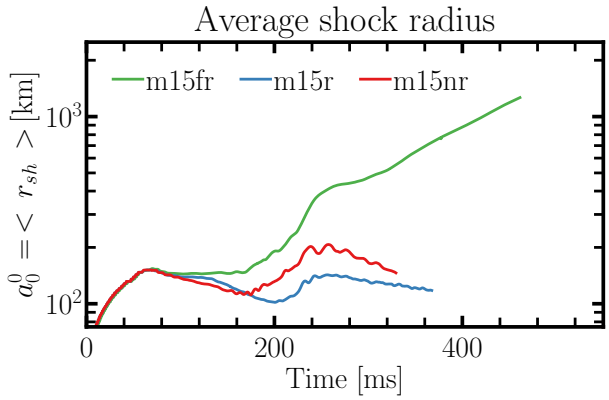

Figure 4. Average shock radius for models m15fr (green), m15r (blue), and m15nr (red) as a function of time after core bounce. The average shock radius is defined as the $(l, m) = (0, 0)$ expansion coefficient of the shock surface into spherical harmonics (Eq. (1)).

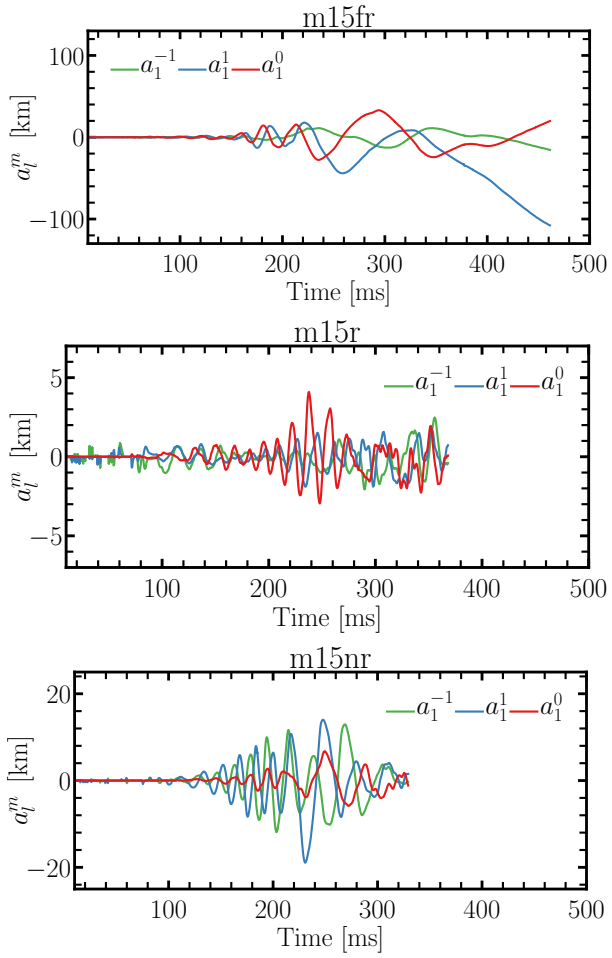

Figure 5. The $(l, m) = (1, 0)$, $(1, 1)$, and $(1, -1)$ coefficients of, the decomposition of the shock surface into spherical harmonics as a function of time after bounce (see Eq. (1)). From top to bottom: model m15fr, model m15r, and model m15nr.

Here

$$\ddot{Q}_{ij} = \mathrm{STF}\left[2\int d^3x\,\rho\,(v_i v_j - x_i\partial_j\Phi)\right]. \tag{4}$$

are the second-order time derivatives of the Cartesian components of the quadrupole moment tensor (with $i, j = 1, 2, 3$) in the TT-gauge, which are given in a form where the time derivatives have been elimated for numerical reason by using the continuity and momentum equations (Oohara et al. 1997; Finn 1989; Blanchet et al. 1990).

The other quantities in Eq.4 are the Cartesian velocity components v_i, the Cartesian coordinates x_i, and the gravitational potential Φ (including post-Newtonian corrections used in the simulations). STF denotes the projection operator onto the symmetric trace-free part.

In the following, we give the GW signal strength not in terms of h_+ and $h_\times$, but in terms of *GW amplitudes* which are defined as

$$A_+ \equiv Dh_+, \qquad A_\times \equiv Dh_\times. \tag{5}$$

These GW amplitudes are convenient because they do not require us to specify the distance D between the observer and the source of the GWs.

Under the assumption of axisymmetry there is only one independent GW component

$$\boldsymbol{h}^{\mathrm{TT}}_{\theta\theta} = \frac{1}{8}\sqrt{\frac{15}{\pi}}\sin^2\vartheta\frac{A^{\mathrm{E2}}_{20}}{D}, \tag{6}$$

where ϑ is the inclination angle of the observer with respect to the axis of symmetry, and A^{E2}_{20} is the only non-zero component of the quadrupole moment. In spherical coordinates A^{E2}_{20} is given by

$$\begin{aligned} A^{\mathrm{E2}}_{20}(t) = \frac{G}{c^4}\frac{16\pi^{3/2}}{\sqrt{15}}\int_{-1}^{1}\int_0^\infty \rho\,\big[v_r^2(3\zeta^2-1)+ \\ v_\theta^2(2-3\zeta^2) - v_\phi^2 - 6v_r v_\theta\zeta\sqrt{1-\zeta^2} \\ -(3\zeta^2-1)r\partial_r\Phi + 3\zeta\sqrt{1-\zeta^2}\partial_\theta\Phi\big]\,r^2\,dr\,d\zeta, \end{aligned} \tag{7}$$

where, ∂_i $(i = r, \theta, \phi)$ and v_i are the derivatives and velocity components, respectively, along the basis vectors of the spherical coordinate system, and ζ is a short hand notation for $\cos\theta$. See, e.g., Müller & Janka (1997) for details.

5 RESULTS

5.1 Qualitative description of the gravitational wave signals

Since the 3D simulations of Summa et al. (2018) do not cover the phase of collapse and bounce, the GW signal emitted during the earlier evolution ($t \lesssim 10$ ms post-bounce) was obtained from their preceding 2D simulations. This part of the GW signal we will discuss later in section 9.

Fig. 6 shows the GW amplitudes generated by asymmetric mass motions for two different observer orientations for the three models of Summa et al. (2018) that we have analyzed. The two columns represent observers located along the pole (left) and in the equatorial plane (right), respectively, of models m15fr, m15r, and m15nr (from top to bottom), *i.e.,* in order of decreasing initial rotation rate. Vertical red dashed lines mark beginning and end of episodes of strong SASI activity. The corresponding amplitude spectrograms are shown in Fig. 7, which we obtained by applying the short-time Fourier transform (STFT) to the corresponding waveforms. To calculate the STFT we moved a window of 50 ms

width across the discrete GW wave amplitude data applying the discrete Fourier transform (DFT) to each window. We define the DFT as

$$\widetilde{X}_k(f_k) = \frac{1}{M}\sum_{m=1}^{M} x_m e^{-2\pi i k m/N}, \tag{8}$$

where x_m is the time series obtained by sampling the underlying continuous signal at M equidistant discrete times, and $f_k = k/T$ is the frequency of bin k with T being the total duration of the analyzed GW signal (50 ms in the considered case). The amplitude spectrograms in Fig. 7 show the square of the STFT amplitudes summed over of the cross and plus polarisation modes, *i.e.,* $|\mathrm{STFT}[A_+]|^2 + |\mathrm{STFT}[A_\times]|^2$. We convolved the GW amplitudes with a Kaiser window (shape parameter $\beta = 2.5$) before we applied the DFT, whereby frequencies below 50 Hz and above 1100 Hz are filtered out.

We find that the GW signals of the two rotating models m15fr and m15r do not differ fundamentally from the signals of the non-rotating model m15nr and those models discussed in Andresen et al. (2017). In all three models considered here, an initial phase of quiescence is followed by a phase of very active, but case-dependent, emission during which the amplitudes are of the order of a few centimeters. As expected, the fast rotating model m15fr emits the strongest GW signal, while unexpectedly the non-rotating model m15nr shows larger amplitudes than the moderately rotating model m15r. Hence, we find no clear correlation between the initial rotation rate and the strength of the GW emission, which might point to considerable stochastic variation. The spectrograms (Fig. 7) of all three models show the low-frequency ($\nu_{\mathrm{GW}} \lesssim 250\,\mathrm{Hz}$) and high-frequency ($\nu_{\mathrm{GW}} \gtrsim 250\,\mathrm{Hz}$) signal components reported by Kuroda et al. (2016) and Andresen et al. (2017).

Note that the signal associated with prompt-convection is present in all three models, but can only be seen in A_+. We suspect that this unexpected behavior is a consequence of an erroneous treatment of fictitious forces in the 2D simulations that evolved the core through bounce (Summa et al. 2018). For this reason angular momentum was not strictly conserved during collapse. This led to slower rotation rates in the inner layers of the core. When the terms switched off by mistake during collapse were taking into account in 3D after core bounce, transient oscillations (caused by the adjustment of the models) affected the first $\sim$ 100 ms after bounce and are the reason why the signals exhibit such peculiar GW emission at early times. The signals during this phase should look more like the ones presented in Andresen et al. (2017).

Model m15fr: The GW signal from model m15fr is characterised by strong emission over a broad range of frequencies. The pronounced low-frequency and high-frequency emission mentioned above is clearly visible (see Fig. 7, upper row), but covering a broader frequency range than in the other two models. At about 200 ms post-bounce the two emission regions almost overlap. When run-away shock expansion is fully underway at $\approx$ 250 ms post-bounce), the overall GW amplitudes strongly decrease, but both low-frequency and high-frequency emission continue to be present until the end of the simulation. Coinciding with the onset of shock expansion, the central SASI frequency starts to decrease around $\approx$ 200 ms after bounce.

Model m15r: With GW amplitudes never exceeding 1.5 cm, this model produces the weakest GW signal of the three models. Furthermore, the signal is strongly reduced in the time period between 180 and 250 ms post-bounce, when the high-frequency emission almost completely subsides and only a very weak low-frequency emission is recognizable. At $\sim$ 250 ms post-bounce the high-frequency emission starts to increase again, while the emission at low-frequencies almost ceases.

Model m15nr: The non-rotating model is characterized by a relatively long initial quiescent phase compared to the two rotating models. This could be a consequence of the lower angular resolution (4 degrees instead of 2 degrees) of this simulation, which delays the growth of convection in the post-shock region. Weak low-frequency GW emission sets in $\sim$ 125 ms after bounce. This low-frequency signal component increases in strength until it reaches a maximum value at $\sim$ 175 ms post-bounce. Approximately 25 ms after the onset of low-frequency emission, high-frequency emission develops at $\sim$ 150 ms post-bounce. Both signal components remain present until the end of the simulation, however, varying considerably in strength.

5.1.1 *Time-integrated energy spectra*

Time-integrated energy spectra, $\mathrm{d}E/\mathrm{d}f$, for each of the models are shown in Fig. 8. These spectra are calculated from the Fourier transform of the second time-derivatives of the Cartesian components of the mass quadrupole moments for every bin k according to

$$\frac{\mathrm{dE}}{\mathrm{d}f} \approx \left[\frac{\Delta E}{\Delta f}\right]_k = \frac{2G}{5c^5}(2\pi f_k)^2 \left|\widetilde{\ddot{Q}^{ij}}_k \widetilde{\ddot{Q}^{ij}}_k\right| T^2. \tag{9}$$

Here T represents the duration of the simulations. See Andresen (2017) for details.

The time-integrated energy spectrum of model m15fr is rather flat, with strong emission over a wide range of frequencies and a local maximum at $\sim 75-100$ Hz. The slower rotating model m15r, which does not develop strong SASI oscillations, emits much less energy at low frequencies, but also exhibits a maximum at $\sim 75-100$ Hz. The maximum, however, is far less pronounced than in model m15fr. The energy spectrum of model m15nr is a hybrid of the spectra of the two other models. As for model m15fr, there is a significant amount of energy radiated away by GW below 300 Hz, but the spectrum is less flat than the one of model m15fr.

6 EXCITATION OF GRAVITATIONAL WAVES

Andresen et al. (2017) studied the GW signals from four 3D simulations of core-collapse supernovae (Tamborra et al. 2013; Hanke et al. 2013; Tamborra et al. 2014b,a; Hanke 2014; Melson et al. 2015), based on three *non-rotating* progenitors. They found that strong SASI activity excites low-frequency GW emission by creating an asymmetric mass distribution in the post-shock layer which directly leads to GW emission. In addition, the high-velocity violent downflows resulting from SASI activity perturb the PNS surface and even the PNS convection layer and excite non-resonant g-modes in the PNS, which in turn lead to strong GW emission. Both the frequency of the forced g-modes in the PNS surface and the mass motions in the post-shock layer are set by the typical time scale of the SASI oscillations as pointed out by Kuroda et al. (2016). Downflows from the post-shock layer onto the PNS also excite resonant surface g-modes and so do convective plumes from the PNS interior overshooting into the outer layer of the PNS (Marek & Janka 2009; Murphy et al. 2009; Müller et al. 2013; Morozova et al. 2018). The propagation of these g-modes is responsible for the high-frequency emission. Andresen et al. (2017) found

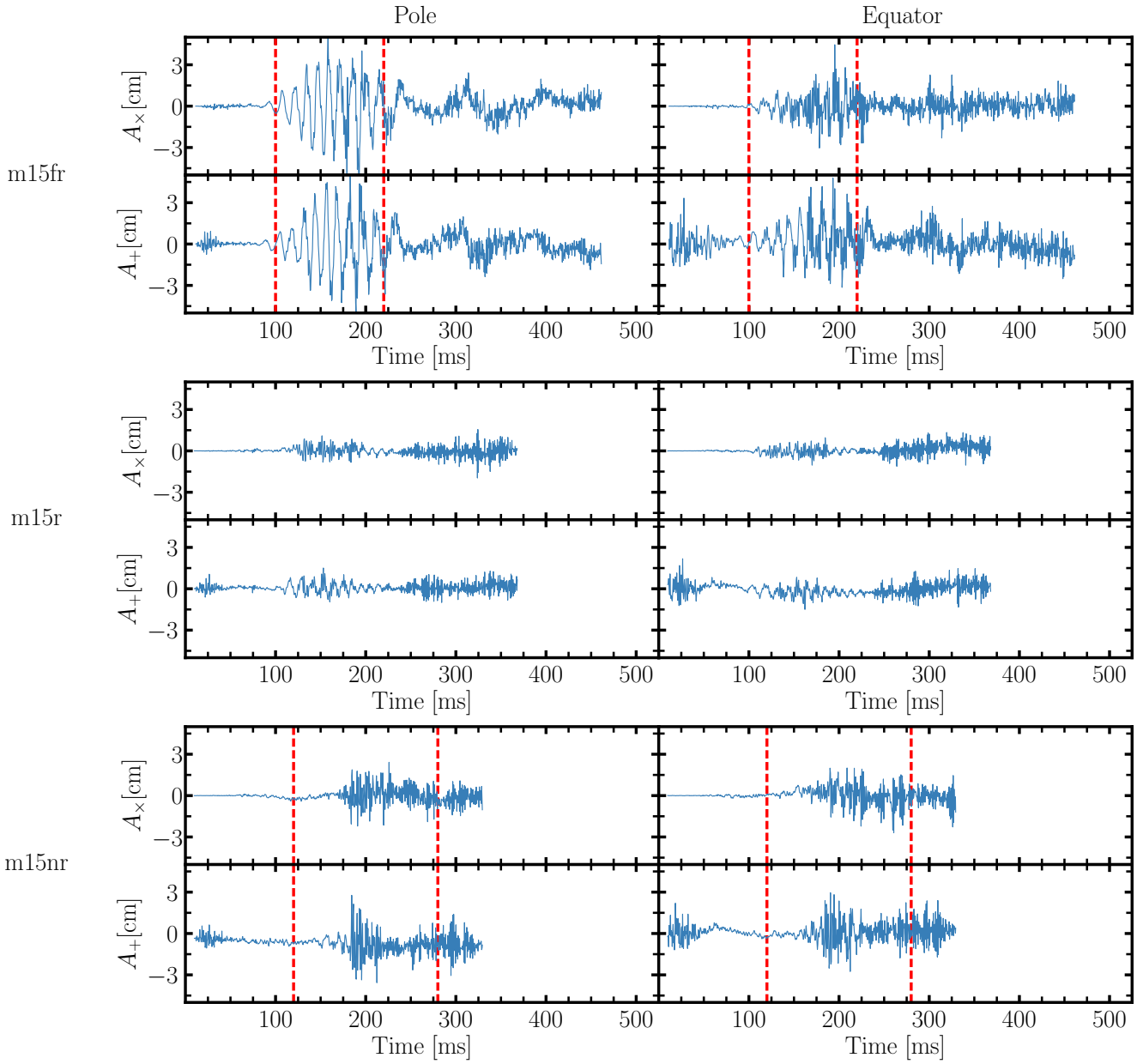

Figure 6. GW amplitudes A_+ and $A_\times$ as functions of time after core bounce for models m15fr, m15r, and m15nr (from top to bottom). The two columns show the amplitudes for an observer situated along the pole (left) and in the equatorial plane (right). Episodes of strong SASI activity occur between the vertical red dashed lines.

that they are mainly excited by PNS convection, with a small contribution from downflows impinging on the PNS surface from above. For the most part, these findings also hold for the three models presented here, but there are two notable exceptions. The GW signal generated by PNS convection ($f_{\rm GW} \gtrsim 300\,{\rm Hz}$) is weak in the two rotating models (see Fig. 7). Additionally, in model m15fr the low-frequency emission ($f_{\rm GW} \lesssim 300\,{\rm Hz}$) generated by mass motions in the post-shock layer (see Fig. 9) is stronger than what was found for the models of Kuroda et al. (2016) and Andresen et al. (2017).

The importance of mass motions in the post-shock layer, with respect to the low-frequency signal, can be seen by dividing the simulation volume into three layers (A, B and C; see also Fig. 4 in Andresen et al. (2017)) and calculating the contributions from each layer to the integral in Eq. (4). Layer A consists of the inner PNS and contains the convectively active layer as well as the region where convective plumes overshoot into the convectively stable PNS surface layer. The second layer, which we call layer B, covers the region extending from the top of layer A to the PNS surface. It should be noted that there are several ways to define the surface of the PNS and that we define it to be where the angle-averaged density drops below 10^{10} g/cm^3. GWs excited by downflows onto the PNS should be emitted, at least in part, from layer B. Layer C encompasses the volume between the PNS surface and the outer boundary of the simulation grid. This outermost layer captures GWs produced by mass motions in the post-shock layer and by matter accreting onto the PNS surface. We refer the reader to Andresen et al. (2017) for a more detailed definition of the three layers.

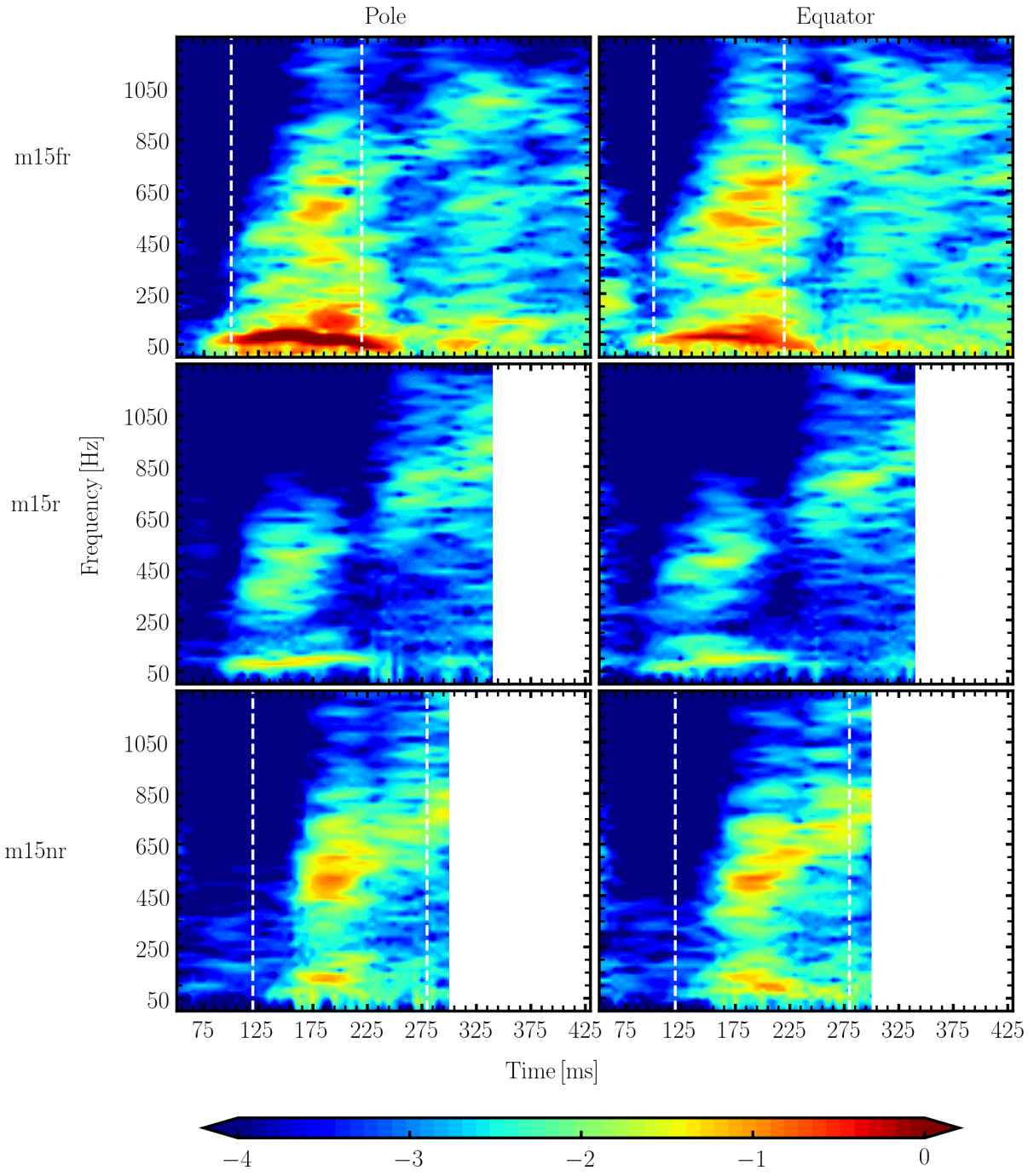

Figure 7. Amplitude spectrograms for a sliding window of 50 ms width summed over the two polarisation modes,*i.e.,* ($|\mathrm{STFT}[A_+]|^2 + |\mathrm{STFT}[A_\times]|^2$). The rows show the results for models m15fr, m15fr, and m15nr (from top to bottom), and the two columns give the amplitudes for an observer situated along the pole (left) and in the equatorial plane (right), respectively. Time is measured in ms after core bounce. Vertical dashed lines bracket SASI episodes. The amplitudes are normalised by the same factor, and their values are colour-coded on a logarithmic scale.

In Fig. 9 we show the spectrograms of the GWs emitted in the three individual layers. It should be emphasised that this plot has to be viewed with caution. Contributions to Eq. (4) from different layers that would normally cancel out can create artefacts. In our simulations, matter is continuously flowing from one layer to another and these non-zero mass fluxes at the boundaries are problematic when calculating the GWs from separate layers. The exact definition of the boundaries becomes important for the strength of individual features in the spectrograms. We have verified that the general picture stays the same when we shift our boundaries, within reasonable limits.

From Fig. 9 we see that the low-frequency emission in model m15fr differs from that found by Kuroda et al. (2016) and Andresen et al. (2017). In model m15fr the strongest contribution to the low-frequency signal comes from layer C, and not from the surface and internal layers of the PNS as reported by Kuroda et al.

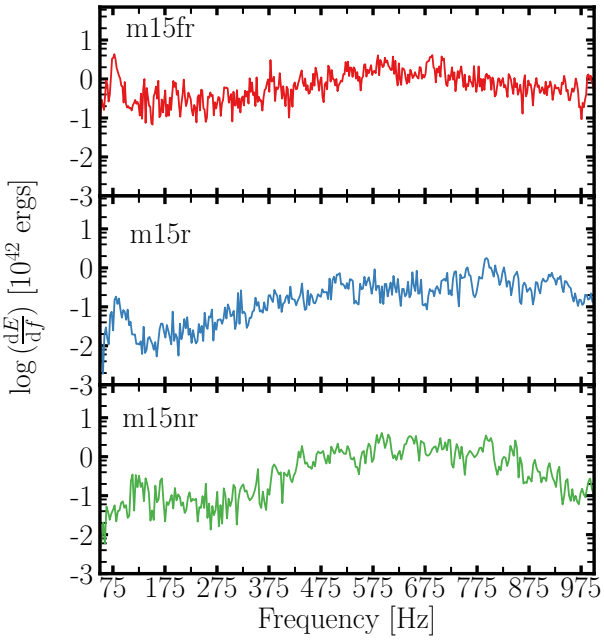

Figure 8. Time-integrated GW energy spectra dE/df for models m15fr, m15r, and m15nr (top to bottom). The spectra are computed for the full time duration of the simulations.

(2016) and Andresen et al. (2017). However, Andresen et al. (2017) concluded that non-negligible contributions to the low-frequency emission arise from each of the three layers, which also holds for the models presented in this work. Because of its temporal coincidence with the SASI episode it is clear that the strong emission from layer C seen in model m15fr is a consequence of the strong spiral SASI oscillations that develop soon after core bounce. The mass accretion rate decreases rapidly as a function of time after bounce (see Fig. 6 of Summa et al. (2018)). The large amount of high-density matter falling through the shock at early times combined with the strong oscillations of the shock should intuitively lead to strong gravitational wave emission produced by mass motions in the layer between the PNS surface and the shock. At later times, when the mass accretion rate drops significantly, or shock expansion sets in, less mass will be involved in mass motions induced by the SASI. Hence, it is reasonable to expect weaker GW emission.

While in the non-rotating model m15nr strong high-frequency emission is clearly visible throughout the whole simulation (see last row of Fig. 7), we see a reduction in the emission above 250 Hz in the rotating model m15r, but the signal component is still clearly visible in the second row of Fig. 7. In the fast rotating model m15fr strong high-frequency emission can be seen at early times, during the SASI phase, but once the SASI subsides the emission is drastically reduced. The emission at early times is caused by SASI-modulated downflows perturbing the PNS surface. A similar behavior was seen in model s20 and model s20s of Andresen et al. (2017). At late times, when the shock expansion is well underway, there is no SASI activity and the mass accretion rate onto the PNS is greatly reduced. In other words, the typical mechanisms that excite oscillations of the PNS from above are absent. The lack of high-frequency emission in model m15fr, at late times (top row of Fig. 7), indicates that PNS convection does not generate strong GW emission. The reduction of high-frequency emission from the PNS convective layer in the two rotating models is connected to the fact that the initial rotation leads to the development of a positive angular momentum gradient in the PNS convective layer. As a result, the PNS convection is weakened according to the Solberg-Høiland criterion (Janka et al. 2001; Buras et al. 2006b). The basic physical picture is that when a buoyant plume propagates outwards, with conserved specific angular momentum, its rotation rate is less than that of the surrounding medium and it experiences a weaker centrifugal force. The result is a net force which acts against the outward propagation of the plume. Angular momentum transfer by convection will eventually flatten the rotation profile within the PNS and the restoring force will gradually decrease with time. By considering the mean field kinetic energy equation, we can see that the average kinetic energy contained in the convective region decreases as we increase the initial rotation rate. It then follows that less energy is injected into the overshooting region and converted into g-modes, which in turn results in a weaker GW signal at high frequencies. In the mean field approach, where the flow is decomposed into average and fluctuating terms, one finds that the kinetic energy sources are buoyancy work due to density fluctuations (W_b) and work resulting from pressure fluctuations (W_p). Viscous forces can also contribute to the overall kinetic energy budget, but the fluid in our simulations is modelled as a non-viscous perfect fluid. If we only consider the radial direction, W_b and W_p can be written as

$$W_b(r) = \overline{\langle g\rho' \, v_r' \rangle}, \tag{10}$$

$$W_p(r) = \overline{\langle p' \, \nabla_r v_r' \rangle}, \tag{11}$$

where ρ', p', and v_r' are the local deviations from the angular averages of density, pressure, and radial velocity (at any given radius), respectively. The gravitational acceleration is represented by g and ∇_r represents the radial part of the divergence operator. The angle brackets denote averaging over all angular bins and the overbar represents time averaging (Hurlburt et al. (1986), Hurlburt et al. (1994), Nordlund et al. (2009), and Viallet et al. (2013)). In Fig. 10 we show W_b and W_p for our three models at three different times. It is clear that the buoyancy work is greatest in model m15nr and smallest in model m15fr. The kinetic energy injected by buoyancy forces decreases with increasing rotation rate. Pressure fluctuations seem to be most important at the bottom of the convective layer, where they act as a net sink of kinetic energy.

Based solely on the damping effect that rotation has on PNS convection, we would expect an overall reduction of high-frequency GW emission in the two rotating models. We would also expect that the fastest rotating model m15fr emits the weakest high-frequency signal. However, the picture is not so simple, because we also have to consider the effects of SASI activity, whose strong influence exerted through a coherent large-scale modulation of the accretion flow onto the PNS effectively perturbs the PNS surface. These perturbations reach into the interior of the PNS and also influence the convective layer of the PNS.

The strong downflows created by the SASI do not only excite non-resonant g-modes in the PNS surface, but also resonant g-mode oscillations. In model m15fr, where the spiral SASI mode dominates the post-shock flow, we see a particularly strong low-frequency signal. This indicates that the spiral mode can effectively perturb the PNS surface. The same behaviour is seen in model s27 and model s20 of Andresen et al. (2017). The PNS surface perturbations, in turn, lead to a stronger resonant g-mode excitation and a stronger high-frequency GW signal. However, because the forcing has a broad spectral distribution, the resulting low-frequency and high-frequency GW emission is also “broadened’. In model m15fr

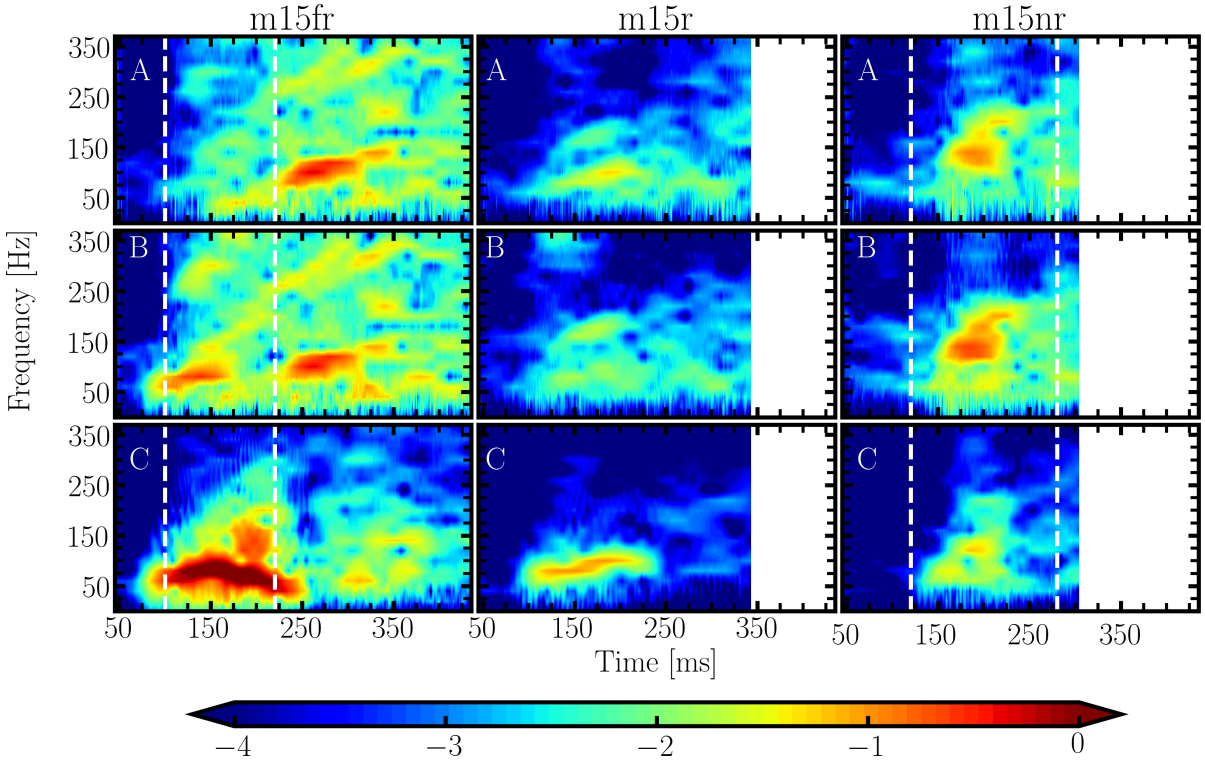

Figure 9. Amplitude spectrograms for a sliding window of 50 ms width summed over the two polarisation modes, ($|\mathrm{STFT}[A_+]|^2 + |\mathrm{STFT}[A_\times]|^2$). The columns show the three different models m15fr, m15r, and m15nr (from left to right). The first row shows the contribution from layer A, the middle row the contribution from layer B, and the bottom row shows the contribution from layer C. Time is measured in ms after core bounce. Vertical dashed lines bracket SASI episodes. The amplitudes are normalised by the same factor and their values are colour-coded on a logarithmic scale. We show the spectrograms for the polar observer direction.

with its strong spiral mode, GWs are emitted over a wider range of frequencies than in model m15r.

The reduction of high-frequency GW emission generated by PNS convection can most clearly be diagnosed in model m15r, in which the average shock radius reaches a minimum at $\sim$ 200 ms post-bounce after a 70 ms long period of recession (Fig. 4). The small average shock radius favours SASI activity over neutrino-driven convection, and we see the development of low-amplitude shock oscillations (Fig. 5, middle panel). Convection, on the other hand, is quenched.

Fig. 11 shows the distribution of the entropy per baryon of model m15r in the equatorial plane at three snapshots after core bounce. In the top and bottom panels one sees the typical hot bubbles that are characteristic of neutrino-driven convection, while in the middle panel such bubbles are considerably suppressed (the same behaviour can be seen in Fig. 3). The growth of low amplitude SASI activity and the suppression of convection in the post-shock layer between $\sim$ 180 and $\sim$ 250 ms post-bounce are reflected in the GW signal as a weak emission at low-frequencies and a complete absence of the high-frequency signal component. At $\sim$ 250 ms post-bounce the high-frequency emission sets in once more, at the same time as the weak SASI oscillations subside.

The SASI activity in model m15r is not strong enough to excite resonant g-modes in the PNS, since we see high-frequency emission during the time when there is no SASI activity, and we see no high-frequency emission during the time when the SASI oscillations are strongest. Moreover, the high-frequency signal vanishes when there is very weak hot-bubble convection in the post-shock layer. It is, therefore, clear that high-frequency emission is caused by convective plumes from the post-shock layer impinging on the PNS surface.

The reduction of GW emitted from the PNS can also be seen in model m15fr. After the onset of shock revival the accretion rate onto the central object decreases and the violent downflows created by strong SASI activity cease to exist. At the same time the GW amplitudes decrease strongly, indicating that excitation of surface g-modes from above the PNS is the main source of high-frequency GW emission. This finding is very different from the behavior of model s20s of Andresen et al. (2017), in which activity within the PNS increased after the onset of shock revival and consequently led to a strong increase of the GW signal amplitude. Thus, the nature of PNS convection, in addition to the flow activity in the post-shock layer, is an important factor in determining the GW signal from core-collapse supernovae.

The spiral SASI mode induces angular mass motions in the outer PNS, which excites low-frequency GWs. The initial rotation of the PNS, which is inherited from the stellar progenitor, is not sufficient enough to have any noteworthy impact on the signals. A rotating triaxial configuration would produce GWs, but the initial rotation of the PNS is not great enough to explain the frequency of the GWs we observe. In Fig. 12 we plot the angle averaged rotation frequency ($\langle f_{\mathrm{rot}} \rangle$) as a function of radius. The rotational frequency of a fluid element around the origin is

$$f_{\mathrm{rot}} = \frac{|\vec{r} \times \vec{v}|}{2\pi r^2}. \tag{12}$$

Here $\vec{r}$ is the position vector and $\vec{v}$ the velocity vector. In spherical

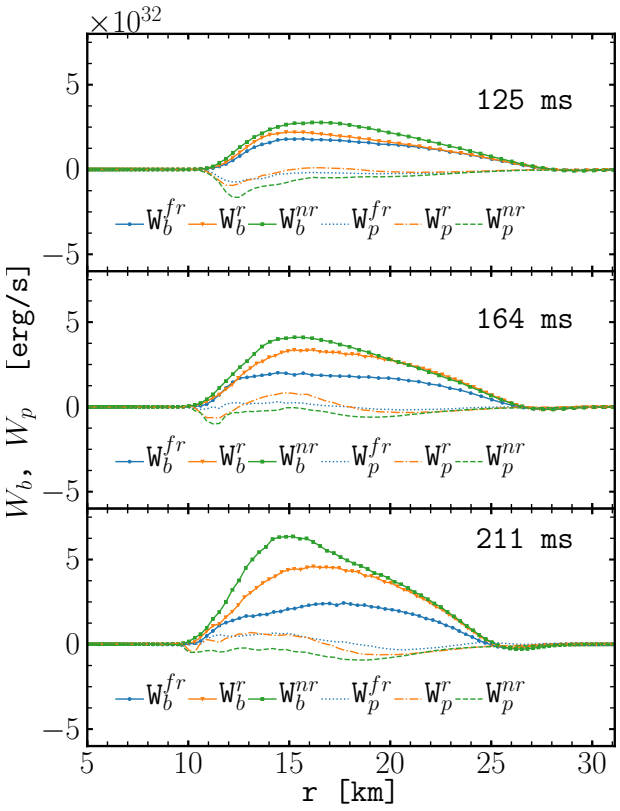

Figure 10. Angle and time averaged buoyancy work due to density fluctuations and work resulting from pressure fluctuations as a function of radius. The time averaging was done over 10 ms. The times shown in the top left corner of each panel indicate the start of the time-window over which the averaging was performed.

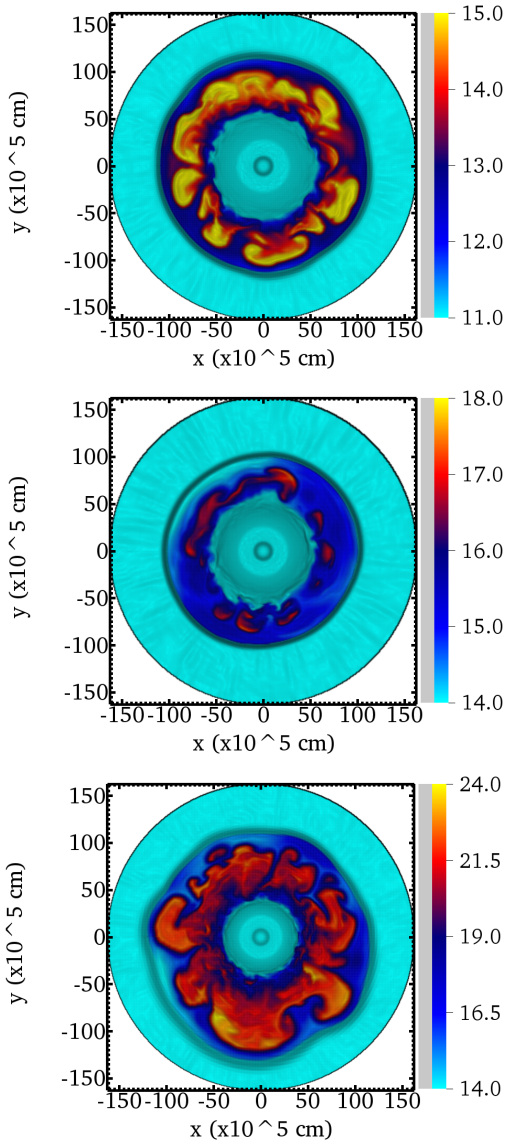

Figure 11. Distribution of entropy per baryon in the equatorial plane for model m15r at 167 (top), 210 (middle), and 343 ms (bottom) post-bounce. The entropy is given in units of Boltzmann's constant k_b.

coordinates the angle average of Eq. (12) is given by

$$\langle f_{\rm rot}\rangle = \frac{1}{4\pi}\int \frac{1}{2\pi r}\sqrt{{v_\theta}^2+{v_\phi}^2}d\Omega, \qquad (13)$$

where v_θ, and v_ϕ are the θ and ϕ components of the velocity vector in spherical coordinates, respectivly. In the first panel of Fig. 12 we see that the rotation rate is initially too low to explain the GW emission. Only later, when the SASI becomes active, are the outer PNS layers spun up sufficiently to account for the low-frequency signal. This argument is also supported by the fact that the low-frequency emission is mainly seen during the SASI phases. The mass motions in the PNS surface, induced by the SASI, continue after the instability subsides. The continued mass motions in the PNS surface are the source of the weak low-frequency emission seen in the spectrograms after periods of strong SASI activity.

In the last panel of Fig. 12 we can see that the average rotation frequency (in the post-shock layer) is greater in model m15nr than in model m15r. The strong SASI activity that develops in model m15nr induces angular mass motions, which at later times causes the post-shock layer fluid of model m15nr to rotate faster than the corresponding fluid in model m15r.

7 DECREASE IN THE CENTRAL SASI FREQUENCY

In the spectrogram (Fig. 7) of model m15fr we can clearly see a decrease in the central SASI frequency after the shock starts to expand. Normally shock expansion leads to rapid decay of SASI activity, but in our fastest rotating model rotation supports the SASI for a few cycles even after shock expansion has started. This does not happen in the non-rotating and exploding model of Andresen et al. (2017). Since the SASI frequency is connected to the average shock radius, we can actually probe the shock expansion using the low-frequency GW emission. More importantly, if we were to observe such an effect it would be a strong indicator that the core of the progenitor was rotating.

The typical frequency of GWs produced by the SASI ($f_{\rm GW}^{\rm SASI}$) can be estimated as follows

$$f_{\rm GW}^{\rm SASI} = \frac{2}{\tau_{\rm SASI}} \approx 2\left[\int_{R_{\rm PNS}}^{R_{\rm S}} dr\left(\frac{1}{c_s}+\frac{1}{|v_r|}\right)\right]^{-1}. \qquad (14)$$

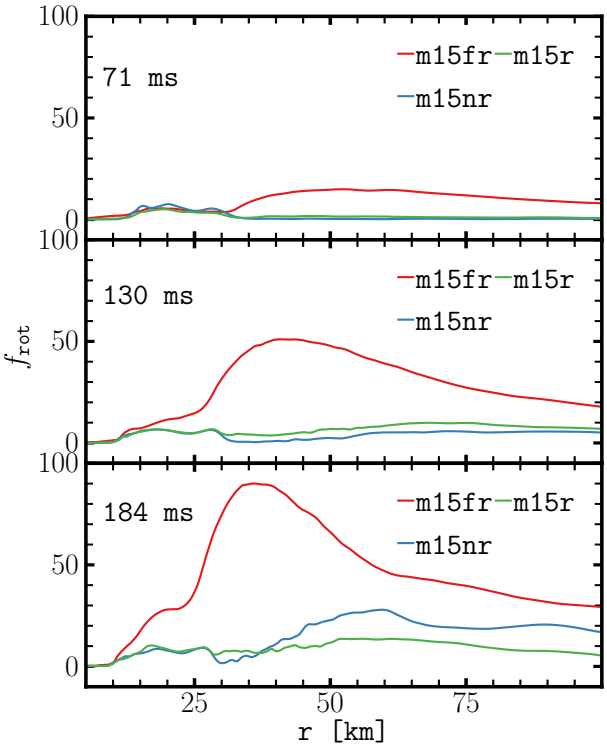

Figure 12. Rotational frequency, defined by Eq. (13), as a function of radius at three different times. The time is given in ms after bounce.

In the above expression $\tau_{\rm SASI}$ is the typical SASI oscillation period, $R_{\rm PNS}$ is the radius of the PNS, $R_{\rm S}$ represents the average shock radius, c_s is the sound speed, and v_r is the typical radial accretion velocity (the advection velocity). We refer to Foglizzo et al. (2007), Scheck et al. (2008), Müller & Janka (2014), and Janka (2017) for more details about the typical SASI time-scale and remind the reader that the factor of two comes from frequency doubling due to the quadrupole nature of GWs.

The advection velocity in the post-shock region is, to first order, a linear function of the radius and given by the post-shock velocity $v_{\rm PS} = -\beta^{-1}\sqrt{GM_{\rm PNS}/R_{\rm S}}$ (β is the ratio of post-shock to pre-shock density and $M_{\rm PNS}$ is the mass of the PNS) as $v_r = v_{\rm PS} r/R_{\rm S}$. Since advection the velocity is typically much smaller than the sound speed, Eq. (14) can be approximately be written as

$$f_{\rm GW}^{\rm SASI} \approx 2\frac{v_{\rm PS}}{R_{\rm S}}\left[\ln\left(R_{\rm S}/R_{\rm PNS}\right)\right]^{-1}. \qquad (15)$$

This means that the ratio of $f_{\rm GW}^{\rm SASI}$ at two different times should be roughly equal to the inverse of the ratio of the average shock radii at the two respective times. (Actually, because of the dependence of $v_{\rm PS}$ on $R_{\rm S}$ and the logarithmic factor the functional variance with $R_{\rm S}$ is a bit steeper). In model m15fr $f_{\rm GW}^{\rm SASI}$ shrinks roughly by a factor of two, from $\sim$ 100 Hz to $\sim$ 40 Hz, during the 100 ms long time window between $\sim$ 150 and $\sim$ 250 ms after core bounce. During the same time window the average shock radius increases from approximately 180 km to 440 km, in other words a factor of around two (see Fig. 7 and Fig. 4). In principle this effect should be visible whenever the shock expands or retreats, but the effect is normally not important because of the relatively small changes in the average shock radius during the SASI dominated phase. However, since the SASI, in model m15fr, persists for a few cycles after shock expansion sets in we can see this effect clearly. In contrast, in the non-exploding models m15nr and m15r, the gradually receding shock front leads to a slowly increasing frequency ($f_{\rm GW}^{\rm SASI}$) of the low-frequency component of the GW emission.

To fully understand how much we can learn about rotation from observing such an effect, it will be necessary to perform several simulations with a wider range of rotation rates and initial conditions and to better understand how the SASI behaves in a rotating medium.

8 THE STANDING ACCRETION SHOCK INSTABILITY, ROTATION, AND RESOLUTION

For the models considered here, there is no clear correlation between the development of SASI activity and the initial rotation rate of the progenitor. Model m15r, in which the rotation rate and profile is in accord with stellar evolution calculations, does not develop strong SASI activity. On the other hand, both the fast rotating model m15fr and the non-rotating model m15nr develop strong SASI activity.

How exactly rotation influences the SASI growth rate and saturation does not seem to be a simple function of progenitor rotation rate. Recently Blondin et al. (2017) studied the effects of rotation by means of idealised hydrodynamic simulations of a standing accretion shock (in 2D and 3D). The results of their study are in good agreement with the perturbative study of Yamasaki & Foglizzo (2008), who found that the linear growth rate of non-axisymmetric SASI modes is an increasing function of the progenitor rotation rate. However, in the non-linear regime Kazeroni et al. (2017) do not find a monotonic connection between the rotation rate and the saturation amplitude of the SASI. In fact, Fig.5 of Kazeroni et al. (2017) indicates that SASI activity may decrease with increasing rotation rate, at least at low to moderate rotation rates. It should be noted that the models of Kazeroni et al. (2017) are idealised simulations which do not include the same physics as the models our work is based on. This leads to different conditions in the post-shock volume and we must, therefore, be careful when extrapolating results from such studies to the models discussed in our work.

An additional complication comes from the fact that model m15nr was simulated with half the angular resolution of the other two models. Lower angular resolution has been found to favour the growth SASI activity, because energy accumulates at larger scales and parasitic instabilities (Rayleigh-Taylor, Kelvin-Helmholtz), which tap energy from SASI motions, are suppressed (Hanke et al. 2012). Abdikamalov et al. (2015) found the opposite, they concluded that decreasing the spatial resolution damps SASI oscillations. However, their simulations were performed with a Cartesian grid and their results could therefore be a consequence of changing the radial resolution in addition to the angular resolution (see Sato et al. (2009)). Independent of whether rotation suppresses the growth of SASI activity in the slowly rotating model m15r or whether SASI activity is enhanced in the non-rotating model m15nr because of insufficient angular resolution, the absence of strong SASI activity in model m15r reduces the overall strength of the GW signal.

9 CORE BOUNCE SIGNAL

Because the 3D simulations of Summa et al. (2018) only start approximately 10 ms after core bounce, the expected GW signal

associated with core bounce is not present in our waveforms in Fig. 6. The evolution of the models from the onset of core-collapse until the start of the 3D simulations was performed by Summa et al. (2018) in 2D, and the resulting GW amplitudes are shown in Fig. 13. The amplitudes (of the two rotating models) are calculated according to Eq. (7).

The flattening of the core that occurs during collapse causes a positive and steadily increasing GW amplitude, in particular in model m15fr. The abrupt halt of the collapse, followed by the expansion of the core leads to a sudden increase in the GW amplitude and a subsequent sharp drop towards negative values. After bounce the waveforms show the typical large oscillations associated with the ring-down of the core, see *e.g.,* Müller (1982); Finn & Evans (1990); Mönchmeyer et al. (1991); Yamada & Sato (1995); Zwerger & Müller (1997). When considering the factor $1/8\sqrt{15/\pi} \approx 0.27$ in Eq. (6), the bounce signal of the two models is slightly (model m15fr) and considerably (model m15r) weaker than the emission from the signal of the post-bounce phase.

10 DETECTION PROSPECTS

Following the procedure laid out in Andresen et al. (2017), we use the signal-to-noise ratio (SNR) (see for example Flanagan & Hughes (1998)) for a matched filtered signal to provide a rough assessment of the detectability of the GW signals described in this work. Under the asumptions of an optimally orientated detector and that the emission is more or less isotropic the SNR for a matched filter signal is given by

$$(\mathrm{SNR})^2 = 4\int_0^\infty df \frac{|\tilde{h}(f)|^2}{S(f)} = \int_0^\infty df \frac{h_c^2}{f^2 S(f)}, \qquad (16)$$

where

$$h_c = \sqrt{\frac{2G}{\pi^2 c^3 D^2}\frac{dE}{df}} \qquad (17)$$

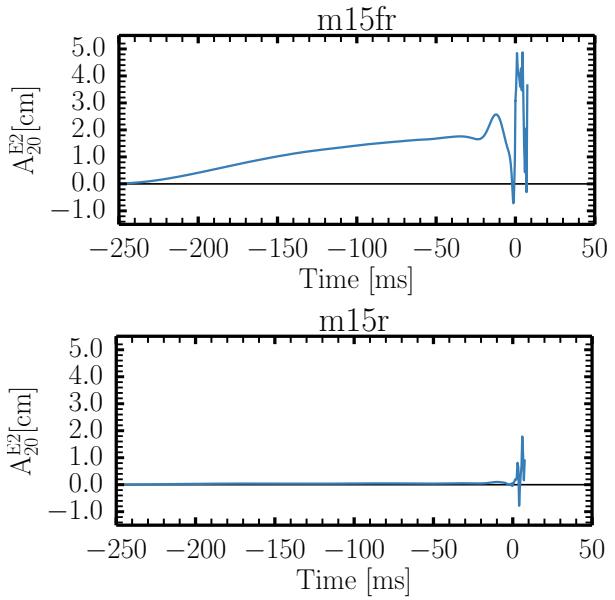

Figure 13. GW amplitudes from 2D simulations of collapse and bounce of models m15fr (top), and m15r (bottom). The amplitudes are calculated according to Eq. (7).

is the characteristic strain and $S(f)$ is the power-spectral density of the detector noise as a function of frequency f. The assumption of isotropic emission alows us to replace $\tilde{h}(f)$ in Eq. (16) with h_c. In reality $\tilde{h}(f)$ will depend on the observer position, but for the purpose of rough estimates these variations are small enough to justify the assumption of isotropic emission. We can, therefore, express the SNR in terms of the GW energy spectrum, which is calculated according to Eq. (9)

We will calculate the SNR in three frequency bands, these bands are the same that were used by Andresen et al. (2017). This allows us to easily compare the results and gauge the effect of rotation. It is particularly interesting to determine whether or not excess of power at low frequencies remains a fingerprint of strong SASI activity in the models presented here, as has been found to be the case for non-rotating 3D models (Kuroda et al. 2016; Andresen et al. 2017). The three bands are defined by the following frequency ranges: 20 . . . 250 Hz, 250 . . . 1200 Hz, and 20 . . . 1200 Hz. These three bands together with Eq. (16) define

$$\begin{aligned}(\mathrm{SNR_{low}})^2 &= \int_{20}^{250} df \frac{h_c^2}{f^2 S(f)},\\ (\mathrm{SNR_{high}})^2 &= \int_{250}^{1200} df \frac{h_c^2}{f^2 S(f)},\\ \text{and } (\mathrm{SNR_{total}})^2 &= \int_{20}^{1200} df \frac{h_c^2}{f^2 S(f)}. \end{aligned} \qquad (18)$$

We calculate the SNR for the zero-detuning-high power configuration of Advanced LIGO (LIGO Laboratory & Shoemaker 2010), and the B (Hild et al. 2008) and C (Hild et al. 2010) configuration for the Einstein telescope. These configurations are referred to as as AdvLIGO, ET-B and ET-C.

From table 1, it is clear that the SNR does not increase with the initial rotation rate of the progenitor. The trend is rather that the SNR correlates with SASI activity. Model m15fr that develops the strongest SASI activity also has the highest SNR, in all bands and for all detectors. Our non-rotating model (m15nr) also develops strong SASI activity and shows higher SNR than model m15r. It should be pointed out that model m15nr, despite its lower angular resolution, is not largely different from the other non-rotating models investigated by Andresen et al. (2017). In model m15r we see the lowest SNR values and only weak SASI activity. However, the ratio of $\mathrm{SNR_{low}}/\mathrm{SNR_{high}}$ is greater for model m15r than for model m15nr. This happens because of the reduced high-frequency emission in model m15r due to dampening of PNS convection by rotation. It is not strong low-frequency emission in model m15r that gives rise to the high ratio of $\mathrm{SNR_{low}}/\mathrm{SNR_{high}}$, high compared to model m15nr, but rather the weak high-frequency emission. In model m15fr the effect is opposite, strong low-frequency emission paired with reduced high-frequency emission gives high ratios of $\mathrm{SNR_{low}}/\mathrm{SNR_{high}}$ in all the three detectors. This means that excess energy in the low-frequency band is not such a clear indication of strong SASI activity as initial 3D models suggested.

Another unfortunate consequence of rotation, unless rapid, is the possibility of greatly reduced signal strength. PNS convection and SASI activity are the main drivers of GW emission and rotation can quench both of these processes. As opposed to rapid rotation, moderate rotation can make the signal harder to detect. On the other hand, model m15fr develops a very strong spiral SASI mode and this enhances the detectability of this model. The exact dependence of the growth of SASI activity and initial progenitor rotation will be crucial for predicting the strength of the GW signal.

Table 1. Signal-to-noise ratios for models m15fr, m15r, and m15nr for three different frequency domains: 20 . . . 250 Hz (low), 250 . . . 1200 Hz (high), and 20 . . . 1200 Hz (total). The table gives values for AdvLIGO and the Einstein Telescope. For the latter, we calculate the SNR for two different modes of operation (ET-B and ET-C) assuming a source at a distance of 10 kpc.

	m15fr				m15r				m15nr			
	Low	High	Total	Low/High	Low	High	Total	Low/High	Low	High	Total	Low/High
AdvLIGO	10.8	4.9	11.9	2.20	2.6	2.4	3.5	1.08	3.5	4.3	5.5	0.81
ET-C	133.2	67.6	149.4	1.97	32.2	34.4	47.1	0.93	46.5	59.3	75.2	0.78
ET-B	224.6	83.5	239.6	2.69	53.7	41.1	67.7	1.30	74.0	72.0	103.2	1.02

10.1 Future improvements

The back of the envelope estimates presented in our work are based on detecting an excess of power in given frequency bands. Our results are in good agreement with standard search methods (Gossan et al. 2016; Abbott et al. 2016b; Powell et al. 2017) that rely on excess power in the detectors during an astrophysically motivated time period. Currently, it seems that the detection of GWs from core-collapse supernovae should not be expected beyond a few kpc. However, signal recovery methods can be improved by incorporating known information about the expected signal into the analysis. While the time domain GW signal is stochastic there are clear patterns in the spectrograms (Fig. 7). The time-frequency evolution of the high-frequency emission is one example of a distinct and robust signal feature. By preferentially searching for signal contributions characterized by phenomenological time-frequency tracks motivated by theoretical predictions, the detection prospects may be improved. Third-generation interferometers will possess noise floors with about one order of magnitude improvement in the amplitude of the design Advanced-LIGO noise floor, which is already a factor of two better than the second LIGO-Virgo (Abbott et al. 2016a, 2017) observing run. The improved sensitivity of the next generation of detectors and advancements in data analysis should extend the detection horizon of GWs from core-collapse supernovae well beyond the estimates presented in this work.

11 CONCLUSION AND DISCUSSION

In this work, we studied how progenitor rotation in 3D models affects the GW signal of core collapse supernovae. We have not studied very rapidly rotating models, but rather focused on the regime of more moderate progenitor rotation. Our main findings are:

(i) Moderate rotation does not change the frequency structure of the GW signal, compared to the signal from non-rotating models. We see the familiar two-component structure with a high-frequency and a low-frequency signal component (Andresen et al. 2017).

(ii) We find that the high-frequency emission instigated by PNS convection is weaker in the rotating models because rotation has a stabilising effect on PNS convection and decreases the amount of energy dissipated in the overshooting region of the PNS. This becomes particularly apparent in model m15r, where we find a strong reduction of the GW amplitudes during a period of time when post-shock convection is weak. The generally weak amplitudes in this model, which has no strong SASI activity, reaffirm the fact that post-shock convection is a weak source of GW excitation, compared to PNS convection and SASI activity.

(iii) Of the three models presented in this chapter the fastest rotating model emits the strongest GW signal because it develops the strongest spiral SASI mode. Based on the models presented here one should not conclude that the strength of the signal will increase with increasing progenitor rotation rate. The conclusion should instead be that the stronger the spiral mode of the SASI is the larger are the amplitudes of the GW signal. However, it remains unclear whether faster rotation in a monotonic dependence leads to stronger SASI activity.

(iv) It should be emphasised that model m15r, where the rotation rate is exactly in accordance with stellar evolution calculations, shows the weakest GW signal.

(v) Unlike model s20s of Andresen et al. (2017), the GW signal of model m15fr decreases after the onset of shock revival. This reduction is due to the small contribution to the total signal from mass motions instigated by PNS convection.

Prior to this work, the GW signals of rapidly rotating models have been studied by several authors (Müller 1982; Rampp et al. 1998; Shibata & Sekiguchi 2005; Ott et al. 2005; Scheidegger et al. 2010a; Kuroda et al. 2014; Takiwaki et al. 2016). A common feature of these studies is that they tend to predict rather strong emission of gravitational radiation. During the post-bounce phase, rapid rotation can lead to the development of novel flow patterns that are not observed in slowly/non-rotating models. Rampp et al. (1998) and Shibata & Sekiguchi (2005) found that very rapid rotation can lead to a bar-like deformation of the central core. In the somewhat slower rotating models of Ott et al. (2005), Kuroda et al. (2014), and Takiwaki et al. (2016) the development of a low-mode spiral instability (low-T/W) was found. While the rotation rate of model m15fr exceeds the threshold found in the simplified models of Kazeroni et al. (2017), where a co-rotation instability can develop, we found no signs of the low-T/W instability in our models (Summa et al. 2018). It is not clear that exceeding this threshold guarantees the development of the spiral mode (Foglizzo 2017). The results from idealised studies should be applied to our models only with caution.

These asymmetric and rapidly rotating structures lead to strong GW emission. It is, however, not likely that a large fraction of the core collapse supernova progenitors have rapidly rotating, or even moderately rotating, cores. Observations of pulsars put strong constraints on the rotation rate of core-collapse progenitors. It has been estimated that most pulsars are formed with rotation periods of a few tens to hundreds of milliseconds (Vranesevic et al. 2004; Popov & Turolla 2012; Noutsos et al. 2013). The recent study by Kazeroni et al. (2017) concludes that the one armed-spiral instability (Ott et al. 2005; Kuroda et al. 2014; Takiwaki et al. 2016) is not able to spin down the PNS enough to make rapidly rotating progenitors compatible with the spin rate of young pulsars. Additionally, stellar evolution models which include the effects of magnetic fields predict slowly rotating stellar cores (Heger et al. 2005). Results from asteroseismology (Beck et al. 2012; Mosser et al. 2012) indicate that the cores of low-mass red giants rotate slower than what is expected from stellar evolution calculations (Cantiello et al. 2014; Deheuvels et al. 2014). According to results from asteroseismology, angular momentum loss due to stellar winds seems to play

a bigger role than currently predicted by stellar evolution calculations (Cantiello et al. 2014).

The rotation rates of the two rotating models studied here are more along the lines of what is expected from state of the art stellar evolution calculations (Heger et al. 2005) and observations (Beck et al. 2012; Mosser et al. 2012; Popov & Turolla 2012; Noutsos et al. 2013; Cantiello et al. 2014; Deheuvels et al. 2014). We find no qualitative difference in the GW signals from the rotating models, compared to those from the non-rotating models in Andresen et al. (2017). We must, therefore, conclude that a stochastic signal with amplitudes of a few centimetres seems to be the generic core-collapse GW signal. Hence, moderate to low progenitor rotation will not significantly increase the detectability of GWs from core-collapse supernovae. Rotation can actually make it more difficult to detect the GW signal, because we find that rotation decreases the signal emitted due to PNS convection in model m15r and consequently makes the model harder to detect.

The fact that model m15nr, the non-rotating one, has an angular resolution that is two times lower (four versus two degrees) than that of the two other models makes it difficult to draw strong conclusions about how the low-frequency signal changes with increasing rotation. It is not clear why model m15nr develops strong SASI activity and model m15r does not. Previously, lower angular resolution in polar coordinates has been found to favour (Hanke et al. 2012) and lower Cartesian resolution to suppress (Abdikamalov et al. 2015) the development of strong SASI activity. At the same time, it is also possible that rotation quenches the growth of SASI activity in model m15r. This is an issue that will have to be resolved by a more systematic study, where the rotation rate and grid resolution are varied independently to discriminate the impact of the individual effects. Since model m15nr, despite its lower resolution, does not behave dissimilar from the non-rotating models described in Andresen et al. (2017), it is possible that a considerable stochastic element plays a role. Another weakness of our study is that the three models all start from a spherically symmetric progenitor model. However, it is not realistic to expect the progenitor stars to be perfectly spherically symmetric objects. In fact, it has been found that asymmetries in the convective burning shells of the progenitor can influence the shock dynamics and even help to ensure a successful explosion (Burrows & Hayes 1996; Fryer et al. 2004; Arnett & Meakin 2011; Couch & Ott 2013; Müller & Janka 2015; Müller et al. 2017). Inhomogeneities in the stellar core could lead to a sizable emission of GWs during the collapse and right after core bounce. Thus, the long period of quiescence after bounce could be an artifact of the usage of spherically symmetric progenitors.

12 ACKNOWLEDGEMENTS

We thank A. Döring for the visualizations of Figures 2 and 3. We also thank T. Melson for helpful discussions about the underlying hydro-data. This work was supported by the Deutsche Forschungsgemeinschaft through SFB 1258 "Neutrinos and Dark Matter in Astro- and Particle Physics (NDM)" and the Excellence Cluster Universe EXC 153, and by the European Research Council through ERC-AdG No. 341157-COCO2CASA. The supernova simulations were performed using high-performance computing resources (Tier-0) on SuperMUC at the Leibniz Supercomputing Centre (LRZ) provided by the Gauss Centre for Supercomputing (GCS@LRZ; LRZ project ID: pr74de).

References

Abbott B. P., et al., 2016a, Classical and Quantum Gravity, 33, 134001
Abbott B. P., et al., 2016b, Phys. Rev. D, 94, 102001
Abbott B. P., et al., 2017, Classical and Quantum Gravity, 34, 044001
Abdikamalov E., et al., 2015, ApJ, 808, 70
Andresen H., 2017, PhD thesis, Technische Universtiät München
Andresen H., Müller B., Müller E., Janka H.-T., 2017, MNRAS, 468, 2032
Arnett W. D., Meakin C., 2011, ApJ, 733, 78
Beck P. G., et al., 2012, Nature, 481, 55
Blanchet L., Damour T., Schäfer G., 1990, MNRAS, 242, 289
Blondin J. M., Gipson E., Harris S., Mezzacappa A., 2017, ApJ, 835, 170
Buras R., Rampp M., Janka H.-T., Kifonidis K., 2006a, A&A, 447, 1049
Buras R., Janka H.-T., Rampp M., Kifonidis K., 2006b, A&A, 457, 281
Burrows A., Hayes J., 1996, Physical Review Letters, 76, 352
Cantiello M., Mankovich C., Bildsten L., Christensen-Dalsgaard J., Paxton B., 2014, ApJ, 788, 93
Cerdá-Durán P., DeBrye N., Aloy M. A., Font J. A., Obergaulinger M., 2013, ApJ, 779, L18
Colella P., Woodward P. R., 1984, *J. Comp. Phys.*, 54, 174
Couch S. M., Ott C. D., 2013, ApJ, 778, L7
Deheuvels S., et al., 2014, A&A, 564, A27
Dimmelmeier H., Font J. A., Müller E., 2002, A&A, 393, 523
Dimmelmeier H., Ott C. D., Janka H.-T., Marek A., Müller E., 2007, Phys. Rev. Lett., 98, 251101:1
Dimmelmeier H., Ott C. D., Marek A., Janka H.-T., 2008, Phys. Rev. D, 78, 064056:1
Finn L. S., 1989, in Evans C. R., Finn L. S., Hobill D. W., eds, Frontiers in Numerical Relativity. Cambridge University Press, Cambridge (UK), pp 126–145
Finn L. S., Evans C. R., 1990, ApJ, 351, 588
Flanagan É. É., Hughes S. A., 1998, Phys. Rev. D, 57, 4535
Foglizzo T., 2017, New insights on the low T/W instability in shocked accretion flows, CoCoNUT 2017 meeting: `https://www.uv.es/coconut/Garching2017/talks/Foglizzo.pdf`
Foglizzo T., Galletti P., Scheck L., Janka H.-T., 2007, ApJ, 654, 1006
Fryer C. L., New K. C. B., 2011, Living Reviews in Relativity, 14, 1
Fryer C. L., Holz D. E., Hughes S. A., 2004, ApJ, 609, 288
Fryxell B., Arnett D., Müller E., 1991, ApJ, 367, 619
Gossan S. E., Sutton P., Stuver A., Zanolin M., Gill K., Ott C. D., 2016, Phys. Rev. D, 93, 042002
Hanke F., 2014, PhD thesis, Technische Universtiät München
Hanke F., Marek A., Müller B., Janka H.-T., 2012, ApJ, 755, 138
Hanke F., Müller B., Wongwathanarat A., Marek A., Janka H.-T., 2013, ApJ, 770, 66
Hayama K., Kuroda T., Nakamura K., Yamada S., 2016, Physical Review Letters, 116, 151102
Heger A., Woosley S. E., Spruit H. C., 2005, ApJ, 626, 350
Hild S., Chelkowski S., Freise A., 2008, preprint, (`arXiv:0810.0604`)
Hild S., Chelkowski S., Freise A., Franc J., Morgado N., Flaminio R., DeSalvo R., 2010, Classical and Quantum Gravity, 27, 015003
Hurlburt N. E., Toomre J., Massaguer J. M., 1986, ApJ, 311, 563
Hurlburt N. E., Toomre J., Massaguer J. M., Zahn J.-P., 1994, ApJ, 421, 245
Janka H.-T., 2017, Neutrino-Driven Explosions. p. 1095, doi:10.1007/978-3-319-21846-5_109
Janka H.-T., Kifonidis K., Rampp M., 2001, in Blaschke D., Glendenning N. K., Sedrakian A., eds, Lecture Notes in Physics, Berlin Springer Verlag Vol. 578, Physics of Neutron Star Interiors. p. 363 (`arXiv:astro-ph/0103015`)
Kazeroni R., Guilet J., Foglizzo T., 2017, MNRAS, 471, 914
Kotake K., 2013, Compte Rendu, 468
Kotake K., Yamada S., Sato K., 2003, Phys. Rev. D, 68, 044023
Kotake K., Iwakami-Nakano W., Ohnishi N., 2011, ApJ, 736, 124
Kuroda T., Takiwaki T., Kotake K., 2014, Phys. Rev. D, 89, 044011
Kuroda T., Kotake K., Takiwaki T., 2016, ApJ, 829, L14
Kuroda T., Kotake K., Hayama K., Takiwaki T., 2017, ApJ, 851, 62
LIGO Laboratory Shoemaker D., 2010, Advanced LIGO anticipated sensitivity curves, `https://dcc.ligo.org/LIGO-T0900288/`

public
Lattimer J. M., Swesty F. D., 1991, *Nucl.~Phys.~A*, 535, 331
Marek A., Janka H., 2009, ApJ, 694, 664
Marek A., Dimmelmeier H., Janka H.-T., Müller E., Buras R., 2006, A&A, 445, 273
Melson T., Janka H.-T., Bollig R., Hanke F., Marek A., Müller B., 2015, ApJ, 808, L42
Mönchmeyer R., Schaefer G., Müller E., Kates R. E., 1991, A&A, 246, 417
Morozova V., Radice D., Burrows A., Vartanyan D., 2018, ApJ, 861, 10
Mosser B., et al., 2012, A&A, 548, A10
Müller E., 1982, A&A, 114, 53
Müller B., 2017, preprint, (arXiv:1703.04633)
Müller E., Janka H.-T., 1997, A&A, 317, 140
Müller B., Janka H.-T., 2014, ApJ, 788, 82
Müller B., Janka H.-T., 2015, MNRAS, 448, 2141
Müller E., Fryxell B., Arnett D., 1991, A&A, 251, 505
Müller B., Janka H.-T., Marek A., 2013, ApJ, 766, 43
Müller B., Melson T., Heger A., Janka H.-T., 2017, MNRAS, 472, 491
Murphy J. W., Ott C. D., Burrows A., 2009, ApJ, 707, 1173
Nakamura T., Oohara K., 1989, in Evans, C. R., Finn, L. S., & Hobill, D. W. ed., Frontiers in Numerical Relativity. Cambridge University Press, pp 254–280
Nordlund Å., Stein R. F., Asplund M., 2009, Living Reviews in Solar Physics, 6, 2
Noutsos A., Schnitzeler D. H. F. M., Keane E. F., Kramer M., Johnston S., 2013, MNRAS, 430, 2281
Oohara K.-i., Nakamura T., Shibata M., 1997, Progress of Theoretical Physics Supplement, 128, 183
Ott C. D., 2009, Classical and Quantum Gravity, 26, 063001
Ott C. D., Ou S., Tohline J. E., Burrows A., 2005, ApJ, 625, L119
Ott C. D., Dimmelmeier H., Marek A., Janka H.-T., Hawke I., Zink B., Schnetter E., 2007, Physical Review Letters, 98, 261101
Ott C. D., et al., 2011, Physical Review Letters, 106, 161103
Ott C. D., et al., 2012a, Phys. Rev. D, 86, 024026
Ott C. D., et al., 2012b, Phys. Rev. D, 86, 024026
Popov S. B., Turolla R., 2012, Ap&SS, 341, 457
Powell J., Szczepanczyk M., Heng I. S., 2017, Phys. Rev. D, 96, 123013
Rampp M., Janka H.-T., 2002, A&A, 396, 361
Rampp M., Müller E., Ruffert M., 1998, A&A, 332, 969
Sato J., Foglizzo T., Fromang S., 2009, ApJ, 694, 833
Scheck L., Janka H.-T., Foglizzo T., Kifonidis K., 2008, A&A, 477, 931
Scheidegger S., Whitehouse S. C., Käppeli R., Liebendörfer M., 2010a, Classical and Quantum Gravity, 27, 114101
Scheidegger S., Käppeli R., Whitehouse S. C., Fischer T., Liebendörfer M., 2010b, A&A, 514, A51
Shibata M., Sekiguchi Y.-I., 2004, Phys. Rev. D, 69, 084024:1
Shibata M., Sekiguchi Y.-I., 2005, Phys. Rev. D, 71, 024014:1
Summa A., Janka H.-T., Melson T., Marek A., 2018, ApJ, 852, 28
Takiwaki T., Kotake K., 2018, MNRAS, 475, L91
Takiwaki T., Kotake K., Suwa Y., 2016, MNRAS, 461, L112
Tamborra I., Hanke F., Müller B., Janka H.-T., Raffelt G., 2013, Physical Review Letters, 111, 121104
Tamborra I., Raffelt G., Hanke F., Janka H.-T., Müller B., 2014a, Phys. Rev. D, 90, 045032
Tamborra I., Hanke F., Janka H.-T., Müller B., Raffelt G. G., Marek A., 2014b, ApJ, 792, 96
Viallet M., Meakin C., Arnett D., Mocák M., 2013, ApJ, 769, 1
Vranesevic N., et al., 2004, ApJ, 617, L139
Yamada S., Sato K., 1995, ApJ, 450, 245
Yamasaki T., Foglizzo T., 2008, ApJ, 679, 607
Yokozawa T., Asano M., Kayano T., Suwa Y., Kanda N., Koshio Y., Vagins M. R., 2015, ApJ, 811, 86
Zwerger T., Müller E., 1997, A&A, 320, 209